In vivo characterization and analysis of glioblastoma at different stages using multiscale photoacoustic molecular imaging

Jinde Zhang
Xiamen University
Xiang Sun
Xiamen University
Honghui Li
Guangdong Academy of Medical Sciences: Guangdong Provincial People's Hospital
Haosong Ma
Xiamen University
Fei Duan
Xiamen University
Zhiyou Wu
Xiamen University
Bowen Zhu
Guangdong Academy of Medical Sciences: Guangdong Provincial People's Hospital
Ronghe Chen
Xiamen University
Liming Nie (nieliming@gdph.org.cn)
Guangdong Academy of Medical Sciences: Guangdong Provincial People's Hospital
https://orcid.org/0000-0002-1781-4612

Research Article

Keywords: Multiscale photoacoustic imaging, Brain tumor, Vascular quantitative analysis, Blood-Brain Barrier, Immune environment

Posted Date: May 5th, 2022

DOI: https://doi.org/10.21203/rs.3.rs-1588501/v1

Abstract

Simultaneous spatio-temporal description of tumor microvasculature, blood-brain barrier, and immune activity is pivotal to understanding the evolution mechanisms of highly aggressive glioblastoma, one of the most common primary brain tumors in adults. However, the existing intravital imaging modalities are still difficult to achieve it in one step. Here, we present a dual-scale multi-wavelength photoacoustic imaging approach cooperative with/without unique optical dyes to overcome this dilemma. Label-free photoacoustic imaging depicted the multiple heterogeneous features of neovascularization in tumor progression. In combination with classic Evans blue assay, the microelectromechanical system based photoacoustic microscopy enabled dynamic quantification of BBB dysfunction. Concurrently, using self-fabricated targeted protein probe (αCD11b-HSA@A1094) for tumor-associated myeloid cells, unparalleled imaging contrast of cells infiltration associated with tumor progression was visualized by differential photoacoustic imaging in the second near-infrared window at dual scale. Our photoacoustic imaging approach has great potential for tumor-microenvironment visualization to systematically reveal the tumor infiltration, heterogeneity, and metastasis in intracranial tumors.

Introduction

Glioblastoma multiforme (GBM) is the most common and lethal malignant brain tumor with a mere median survival of 12–14 months in current standard of medical care [1]. The rapid invasive growth of tumors into the normal brain parenchyma is a critical cause of mortality by rapid proliferation, angiogenesis promotion, and immunosuppression [2]. The neovascularization and immunosuppressive microenvironment are directly related to tumor progression. Excessive neovascularization is identified as a salient feature in tumor tissues from patients with GBM [3]. These underscore the urgent need for an improved understanding of GBM-caused vascular changes, especially at the microscopic level. To achieve invasion and metastasis, GBM cells initially invade and break the blood-brain barrier (BBB), which is essential for regulating the homeostasis of the normal central nervous system [4]. BBB dysfunction during tumor progression is referred to as the more permeable blood tumor barrier (BTB), which is utilized as an important aspect of brain tumor grading and follow-up existence [5, 6]. The heterogeneous permeability to particles of various size also contributes to suboptimal drug accumulation in brain tumors [7]. Consequently, BBB integrity hinders drug delivery to brain tumors in clinically effective therapy. Visualizing the BBB status is a promising way to reveal the heterogeneous distribution of drugs in the tumor and then enables appropriate clinical interventions. Conventional BBB evaluation is based on the classic Evans blue (EB) assay with brain tissue *in vitro* [8]. Radiolabeled EB derivatives, for instance, a 1,4,7-triazacyclononane-N, N', N"-triacetin acid conjugate of a truncated form of EB served as a PET tracer to evaluate the enhanced vascular permeability with high sensitivity, but low spatial resolution [9]. A noninvasive, accurate, and longitudinal visualization approach to evaluate the BBB integrity *in vivo* remains elusive.

The immune microenvironment is a key regulator in promoting or impairing primary and metastatic brain malignancies. The BBB is often compromised under various kinds of pathologic statuses that exists a

robust infiltration of multiple immune cell types from the peripheral circulation [10]. Tumor-associated myeloid cells (TAMCs) are the most abundant immune population (up to 30–50% of the tumor cells) involved in tumor stromal cells, which are recognized as major players in the connection between inflammation and tumors [11, 12]. The major components of TAMCs include tumor-associated macrophages and myeloid-derived suppressor cells, which are strongly inhibiting both innate and adaptive immunity [13, 14]. As tumors progress to malignancy, TAMCs produce mediators that shape the tumor microenvironment which stimulates angiogenesis, enhancing tumor cell migration and invasion, and suppresses antitumor immunity [15]. TAMCs inhibition has robust effects on blocking glioma genesis [16]. Although the importance of immune cells in tumor biology has been largely confirmed, there is an urgent need to explore effective imaging methods for *in vivo* immune activity visualization.

Imaging methods that provide multiple features related to tumor progression allow for a more accurate distinction of GBM. Visualizing neovascularization and TAMCs not only provides the pathological changes of GBM for diagnosis, but also reflects effective prognostic indicators for current clinical therapies, for instance, anti-angiogenic and immune-related therapy. However, intravital imaging modality to simultaneously reveal these multi-feature (angiogenesis, BBB dysfunction, and immune environment) remains a dilemma. Techniques such as flow cytometry and proteomics are capable of measuring the TAMCs *in vitro* [17], but lack timeliness and the spatial distribution information *in vivo*. Positron emission tomography (PET), single-photon emission computed tomography (SPECT), computed tomography (CT), and magnetic resonance imaging (MRI) have facilitated the brain tumor diagnosis in clinics [18, 19]. Both SPECT and PET provide deep penetration, but suffer from possible radiation and poor spatial resolution, which limits the microscopic delineation of angiography. Besides, CT is often criticized for its lack of functional information [20, 21]. MRI provides 300 μm resolution but requires a high magnetic field and long data acquisition time [22]. Although optical imaging modalities such as two-photon microscopy can visualize vessels and the activities of the immune cells across multiple cortical layers at high resolution, the field-of-view is relatively small with obligatory usage of exogenous fluorescein. Further, optical microscopy methods suffer intense photon scattering and generally require skull removal or cranial window.

To overcome these dilemmas, we selected photoacoustic imaging (PAI) as a versatile imaging tool for multi-feature detection of GBM, which includes photoacoustic computed tomography (PACT) characterized as a large field of volume and photoacoustic microscopy (PAM) featured with high spatial resolution [23–26]. The hybrid PAI combines the abundant contrast of optical imaging with the high spatial resolution of ultrasonography, enabling structural, functional, and molecular imaging [27, 28]. In the malignant progression of GBM, tumor angiogenesis destroys the original microcirculation system. As a result, the structure and function of tumor neovascularization are imperfect, which affect the integrity of BBB. Therefore, macromolecular substances in the circulatory system can enter the brain parenchyma and at the same time affect the immune microenvironment. In this work, we present a dual-scale multi-wavelength photoacoustic molecular imaging approach for characterization of tumor microvasculature, BBB, and immune activity. Multi-feature quantification of neovascularization was carried out on both macroscopic and microscopic scales. By extending the classic EB assay *in vivo*, dynamic BBB

permeability was quantified by high-resolution PAM. More importantly, using a self-fabricated human serum albumin (HSA) carried second near-infrared (NIR-II) absorption dye (A1094) with targeted antibody (αCD11b) probe (αCD11b-HSA@A1094), our PAI approach depicted tumor microenvironment of intracranial tumors with an unambiguous contrast.

Experiments And Methods

PA imaging setups

The PAM with MEMS scanning module not only ensures high signal-to-noise ratio, but also significantly improves the time resolution of imaging [29-32]. Our MEMS-based mechanical scanning PAM was improved from the previous systems [33, 34]. Briefly, a 532 nm pulsed laser (AONano 532-1-40V, Advanced Optowave Corporation, pulse duration <1.8 ns, pulse-repetition rate: 10 kHz) and a 1064 nm pulsed laser (VOPO-200-20, Elforlight, pulse duration ~7 ns, pulse-repetition rate: 300 Hz) were used as the light source. The laser beams were first integrated into the subsequent shareable optical path by a dichroic mirror, which passed a 532 nm laser beam but reflected a 1064 nm laser beam. A small proportion of the beam was split by the beam splitter into the photodiode for triggering. After beam expanding, the beams were focused and coupled into a 1 m custom-made single-mode fiber and then transmitted to an ultrasonically and optically confocal probe. The collimated laser beam was focused on the cortex by an objective lens (RMS4X, 0.1NA, Thorlabs). An ultrasonic transducer (V214-BB-RM, central frequency: 50 MHz, -6 dB bandwidth: 80%, Olympus) was attached on the side of the optical-acoustic combiner coaxially for PA signal detection. We adopted a design to make the focused light beam and the acoustic beam coaxial (Fig. S1), which maximized the detection sensitivity of the ultrasonic transducer. To achieve 3D PA revealing, the focused beam was scanned by MEMS for fast B-scan imaging. By cooperating with two-dimensional linear stages (Micos PLS-85, PI), the system enables a large field of view (FOV) scanning. The PA signal was amplified by two serially connected amplifiers (ZFL-500LN, Mini-Circuits) with a 50 dB gain. The B-scan rate along the X-axis was jointly determined by step size, scanning length, and the laser pulse repetition frequency (PRF). Accordingly, the B-scan rate is calculated as: B-scan rate = PRF/(2 × pixel numbers). In our MEMS-PAM system, the laser PRF can be set to 100 kHz, so the B-scan rate is 250 Hz (step size: 10 μm, scanning length: 2 mm). In addition, the imaging speed of the system can be further improved by using higher PRF lasers and parameterized for various application scenarios.

When performing cerebrovascular imaging, the PA transducer was immersed in a water tank full of deionized water. The scalp was cut along the midline with a wound of about 2 cm after head-fixing with a home-made holder. The imaging was completed with the skull intact. After hemostasis with a hemostatic sponge, the sterile ultrasound gel was applied to keep the skull moist and reduce the loss of PA signal in propagation. The dual-wavelength PA images were sequentially collected and reconstructed from the data sets by MATLAB (Mathworks, USA). To reduce the impact of focal length shift, we used an anti-reflection (400-1100 nm) achromatic lens for focusing, which initially reduced the focal length shift to ~300 μm. Before *in vivo* imaging, we also conducted an image matching experiment on the phantom

(Fig. S2). The phantom experiment provided an empirical value to balance the focus and acoustic sensitivity of the two wavelengths. 3D volume rendering was performed on Volview (Kitware, USA).

For PACT imaging, the commercial system Vevo LAZR-X (Vevo, Fujifilm, Japan) and Nexus 128 (Endra Life Sciences, USA) were employed. An MX550D linear-array transducer (center frequency: 40 MHz, range: 25-55 MHz) with 970 and 1200 nm laser beam in LAZR-X system was performed to achieve cortex vessel distribution and TAMCs infiltration, respectively. Two straight line scans were performed with a mechanical stage to reconstruct a dual-wavelength 3D image. PA B-scan frames were acquired parallelly and displayed at 5 Hz frame rate. The area of each scan was 10 mm×12 mm with a step size of 0.1 mm. The Nexus 128 system equipped with hemispherical ultrasonic transducer (center frequency: 5 MHz, bandwidth: 70%) array under 800 nm laser (pulse duration ~7 ns, repetition rate: 20 Hz) was used to record the whole cortex vascular morphology alteration in Fig. 2g. The mechanical device facilitated rotation scanning of 120 to 180 positions to reconstruct image with high quality.

Orthotopic xenografting GBM model preparation

U87MG human GBM cell line was purchased from American Type Culture Collection and cultured in Dulbecco's modified Eagle's medium (DMEM, Gibco) supplemented with 10% fetal bovine serum (FBS, Gibco) and 1% Antibiotic-Antimycotic Solution at 37 °C under 5% CO_2 atmosphere. Balb/c nude mice (20 ± 2 g, Xiamen University Laboratory Animal Center) were housed according to standard guidelines with free access to food and water in a 12 h-light/dark cycle.

Mice were anesthetized and maintained with 1.5% vaporized isoflurane. After fixing the head, the skull was exposed by midline incision of scalp in a sterile condition. The cells (10^6 cells/mL) were stereotactically implanted into the mouse brain by a digital pump at an infusion rate of 1 μL/min with Hamilton syringe. After infusion, the syringe needle was selectively moved up 0.5 mm and remained in position for a minimum of 3 min, maximizing infiltration and minimizing the backflow of the injected cell suspension. Mice were inspected daily for symptoms of tumor development. All animal experiments were approved by the Institutional Animal Care and Use Committee approved procedure at Xiamen University.

Vascular morphology analysis

To quantify morphological changes of cortex vessels along with tumor progression, vessel density, vessel number, branch points, and tortuosity were used as features. The data were processed using a customized vascular morphology extraction algorithm based on MATLAB. Briefly, the original photoacoustic images were first filtered and enhanced to obtain an optimized contrast and remove false-negative pixels within the volume of segmented vessels. Next, the blood vessels were segmented through threshold processing and performed image binarization. Based on the extracted binary vessel image, the vessel density can be counted as the ratio of the vessel pixels to the total pixels. Our centerline extraction was based on a multi-stencil fast marching thinning algorithm. Based on the centerlines, we extracted

vessel number, branch points, and tortuosity. The branch points are where large vessels differentiate into multiple small vessels, which are meaningful in reflecting capillaries degenerate and angiogenesis in brain tumors. The tortuosity was calculated as a morphological feature of vessels through the ratio of the linear distance between the start point and the endpoint and the actual length of the centerline. The flowchart of extraction algorithm can be found in Fig. S3. Furthermore, to ensure the comparable region of different stages, we used the method of multiple vascular feature points comparison to register the regions based on MATLAB. Briefly, the repetitive blood vessels and branch points in different stages were determined as feature points. Based on the coordinates of these points, the size and position of the ROIs can be determined by calculating the distance between these points and the edge of the ROIs.

Cerebrovascular permeability analysis

EB dye was used to determine the integrity of the BBB *in vivo*. After the baseline imaging, 2% (w/v) EB dye was injected at a dose of 4 mL/kg animal's body weight. Image acquisition was performed every 15 min within 2 hours after injection. The 532 nm light was used to achieve both high-contrast PA imaging of tumor microvessels and dynamic EB dye extravasation according to the absorption. Dynamic quantification of the BBB permeability was achieved by counting the total number of pixels occupied by the extravascular dye. The vessel pixel number was quantified in the baseline image acquired prior to EB injection. After subtracting the baseline signal, the increase in non-background pixels in the post-injection images was attributed to the dye extravasation. With this, the experimentally measured amount of EB that extravasated out of the cerebral vasculature was fitted by an experimental model [35, 36]:

$$E(t) = A \times (1 - ext(-kt)) \ (1)$$

Where A is the initial amount of dye extravasated from the vasculature, k is the extravasation coefficient. To calculate the extravasation rate equation, the first derivative of the equation can be expressed as:

$$\frac{\partial E(t)}{\partial t} = A \times k \times \exp(-\mathrm{kt}) \ (2)$$

While the experimental mode and extravasation rate equation around the tumor region show different trends, which can be expressed as:

$$E(t) = A \times (ext(kt) - 1) \ (3)$$
$$\frac{\partial E(t)}{\partial t} = A \times k \times \exp(\mathrm{kt}) \ (4)$$

Preparation of αCD11b-HSA@A1094

We synthesized A1094 dye according to the classical two-step method (see Supplementary Methods), then the dye was characterized by ^{1}H, ^{13}C NMR, and mass spectrum (Fig. S4-S7). Compared with the traditional NIR dye ICG, A1094 showed excellent absorption characteristics in the NIR II region (Fig. S8).

To fabricate the target probe, HSA (40 mg) was completely dissolved in PBS (20 mL, pH=7.4). A1094 solution (200 μL, 5 mg/mL) in dimethyl sulfoxide (DMSO) was slowly added into the HSA solution under magnetic agitation. Subsequently, anhydrous methanol (100 μL) and paraformaldehyde (200 μL, 2.5%) were added into the above system and stirred overnight. The HSA@A1094 complex was obtained via ultrafiltration centrifugation and dialysis. On this basis, the complex was then transferred to the PBS solution (pH=8.0), which contained Tris(2-carboxyethyl) phosphine for the protein surface sulfhydryl activation. After that, αCD11b antibodies activated by 2-iminothiolane hydrochloride were mixed with above solution and stirred overnight at 4 °C. Finally, the purified αCD11b-HSA@A1094 probe was obtained with further ultrafiltration centrifugation and dialysis.

MRI for tumor progression

MRI was performed on a Bruker Biospin 9.4 T small animal MRI scanner (Bruker, Germany), which was equipped with a horizontal bore (diameter: 30 cm; gradient strength: 734 mT/m) and fitted mouse brain coil. The mouse was anesthetized and maintained with 1-2% isoflurane in 20% oxygen. T2-weighted axial images were achieved using a fast spin-echo multiple slice sequence with the following parameters: repetition time (TR) = 2500 ms, echo time (TE) = 33 ms, matrix = 256 × 256, FOV = 2.5 cm × 2.5 cm, signal averaging = 2, section thickness = 0.5 mm.

Results

Dual-scale molecular PAI approach for multiple indicators of GBMs

PAI has already shown its structural and functional brain imaging capability in living rodents. The combination of the two PAI modalities, optical-resolution PAM and linear transducer scanning PACT, with endogenous and exogenous agents provided multiple features related to GBM tumor progression at different levels. The schematic diagram of the microelectromechanical system (MEMS) based PAM system was shown in Fig.1a. In brief, two laser beams with wavelengths of 532 and 1064 nm were coupled into a signal-mode fiber and then focused on the tissue. The generated photoacoustic (PA) signals were collected and transmitted by an optical-acoustic combiner and detected by an ultrasonic transducer. Volumetric images were obtained using a fast MEMS-based scanning mirror in combination with a two-axis mechanical stage. The lateral resolution of this PAM system was characterized as 7.3 and 12.4 μm at 532 and 1064 nm, respectively (Fig. S2). To illustrate the imaging capabilities *in vivo*, we imaged the mouse brain through an intact skull with scalp removed. The left image in Fig. 1b showed the vascular distribution on the cortex with an area of 5 mm × 9 mm along the X and Y axis. The cortex vessel was also expressed in a 2D color map with depth encoded in the right image. The superior sagittal sinus (SSS) and transverse sinus (TrS) were differentiated from cortical vasculature marked in Fig. 1b.

To access the extent of BBB dysfunction in tumor progression, the traditional EB assay was ameliorated to evaluate the permeability of cortical vessels. When BBB is intact, EB dye binds to the macromolecular albumin in circulation, but cannot cross the barrier to stain brain parenchyma. Visualizing the EB distribution in the brain parenchyma by PAM can reflect the leakage of BBB at microscopic level (Fig. 1c).

In addition, to better understand the impact of GBM on the brain, we presented a PAI approach for immune microenvironment visualizing by incorporating a second NIR -II photoacoustic agent (A1094) into the HSA carrier with antibody targeting (Fig. 1d). For PACT imaging, an ultrasonic transducer array affiliated with a portable photoacoustic tomography system was scanned linearly to form volumetric images, a rapid differentiation of vascular abnormalities between tumor and ambient normal tissue was achieved in the tumor-bearing brain (Fig. 1e). Taking the advantage of the distinct difference in absorption spectrum between the hemoglobin and probe, the alteration of cortex vasculature and TAMCs infiltration induced by GBM were revealed with 970 and 1200 nm wavelengths (Fig. 1f). Using the dual-scale PAI combined with an intelligent targeting probe at NIR-II window, multi-indexes along with GBM progression were visualized and extracted. The whole PAI approach for GBM visualization and analysis in malignant progression was described in Fig. S9.

Label-free cortex vascular alteration imaging by dual-scale photoacoustic imaging

To visualize tumor progression at various stages, we used a 9.4T MRI (Biospec, Bruker, USA) on an orthotopic GBM tumor model. The T2-weighted axial plane images showed subsequent heterogeneous intensity enhancement of tumor lesions on Day 7, 12, and 18 (1 mm depth). The obvious midline displacement of brain tissue with edema around the lesion was observed on Day 18 (Fig. 2a). The 2 mm depth MRI images identified the brain structure such as hippocampus and tumor location shown in Fig. S10. Correspondingly, the MEMS-based PAM system was used to analyze the microvascular changes at various MRI-confirmed tumor stages. The angiogenesis of the brain tumor was confirmed by positive CD31 stain in the brain slices (Fig. S11). As shown in Fig. 2b, the microvascular morphology was vividly revealed without labeling. The vascular distribution in the tumor region manifested strong spatial heterogeneity and different morphological features with tumor progression. To avoid the combined influence of multiple factors on the whole area assessment, such as reduced blood perfusion and angiogenesis, we selected ROI I and ROI II for vascular quantitative analysis. Multiple parametric analysis was carried out at two regions of interest (ROI I and II), including total vessel numbers (Fig. 2c), density (Fig. 2d), branch points (Fig. 2e), and tortuosity (Fig. 2f). Contrary to ROI II, the number of blood vessels, blood vessel density, branch points, and tortuosity in ROI I all showed a moderate fractional increase as the tumor progressed, especially on Day 18. The number of vascular branches and circulation within ROI I elevated as the complexity of tumor-induced angiogenesis increased. The PA amplitude in ROI II attenuated and all the four parameters except tortuosity decreased with tumor progression, indicating reduced vascular perfusion in the region. The increased tumor volume is always accompanied by compression of surrounding tissue, which may lead to local heterogeneous blood perfusion [37]. The statistical results showed obvious differences in the parameters of multiple vascular characteristics in both ROIs, which explained the highly heterogeneous growth of GBM tumors at microvascular level.

Solid tumor volume increased with the malignant progression, and there were significant mass effects of tumor squeezing normal brain tissue. The tumor mass effects can distort cerebral topography and result in the reorganization of functional networks in a GBM patient. The brain chamber was deformed under pressure, causing the midline structure to shift to the other hemisphere. The distribution of whole-cortex

vessels, especially the vessels along the sagittal suture, was obtained by the PACT and PAM, respectively. At a macroscopic level, PA amplitude was significantly increased at the SSS and tumor region compared to the normal group by PACT. The distribution of blood vessels was more chaotic in the tumor-bearing brain. The spatial occupation of the solid tumor made the cortical vascular hetero-distribution, forming a height difference of 1.5 mm from the baseline (Fig. 2g). Besides, the corresponding microscopic vessel morphology changes along the sagittal suture were revealed by PAM (Fig. 2h). As normal, the vessels inside sagittal suture were hard to distinguish at microscopic level (Fig. 1b). At the advanced tumor stage, blood vessels were squeezed to the cortex shallow by brain tumors. The abnormal perfusion and distorted distribution of blood vessels in the region can be observed as shown by the blue dashed box in Fig. 2g. These results showed remarkable changes in vascular morphology and spatial heterogeneity caused by tumor masses at two scales.

BBB dysfunction caused by tumors in cerebrovascular permeability

The blood-brain barrier is a major guarantee for the maintenance of brain homeostasis. As an important barrier between the brain tissue and the cerebral blood circulation, tumor-induced BBB dysfunction is associated with tumor invasions and therapeutic drug delivery. EB dye bound to serum albumin can cross the dysfunctional BBB and stain the parenchyma. It has been exploited to quantify protein leakage as an indicator of increased vascular permeability. Capitalizing on the strong optical absorption of EB, its extravasation was dynamically imaged and quantified by PAM (Fig. S12). The PA signals maintained a good linear relationship with EB at different concentrations, which ensures the imaging sensitivity of PAM to EB at low concentration. The PA performance of EB was not affected by laser irradiation during imaging (Fig. S13). Then we conducted a BBB integrity assessment for the early, middle, and advanced stages of tumor malignant progression (n=4 for each group). Different stages were grouped by T2-weighted MRI images and the visual contrast difference was also confirmed by the dissected brain tissues in Fig. 3. Fig. 3a revealed the MRI image of GBM-bearing mouse brain at Day 7. PA image of the brain cortex acquired in the yellow dashed box of (a) by PAM at 24 h after EB injection was shown in Fig. 3b. The diffuse signal indicated EB extravasation from the vessels. Much less EB staining was evident in the brain tissue (Fig. 3c). The photos of *ex vivo* brain tissue was shown in Fig. 3d. Corresponding results of GBM-bearing mouse brain at Day 18 were revealed in Fig. 3e-h. Areas of “bluing” in photos represent that the vascular permeability to EB-albumin complex increased with tumor progression. The PAM images of three tumor stages were exhibited in Fig. 3i-3j and Fig. S14-S16. No BBB difference was observed in the first two tumor stages.

Fig. 4a and 4b showed time-lapse PA maximum amplitude projection (MAP) images of the same region in the tumor-bearing mouse brain for 120 min following intravenous injection of EB dye, which indicated a distinct difference between the early (Day 7) and advanced (Day 18) stages of GBM. The PA intensity in the vessels was directly related to the distribution of EB in the body. As the control group, no obvious EB leakage was detected in time-lapse PA images in the normal mouse cortex within 120 min after injection (Fig. S17). To analyze the spatial distribution of EB extravasation over time, three lines in different directions across the tumor region (lines 1, 2, and 3) were plotted to show PA amplitude in tumor region of

Fig. 4a and 4b. These curves reflected the changes of PA amplitude from EB in and out of vessels with time. The peak signal in the curves represented the vessels, while the diffuse signals were caused by increased EB leakage over time. Furthermore, the spatial scale of the diffusely distributed signal also widened with time. In non-vascular areas, the increase of PA signals over time indicated the process of EB extravasated from the vessels and stained the brain tissue. The results showed that no obvious EB extravasation was observed within 120 min in the early-stage GBM model (Fig. 4c). This is consistent with the conclusion that early tumor activity is more dependent upon the original blood vessels for support, and the integrity of BBB remains relatively intact.

However, there was a gradual increase of EB extravasation along with time and striking difference within 120 min of the advanced stage GBM model (Fig. 4d). The regions highlighted by green and blue dashed boxes in the “120 min” image of Fig. 4b were selected as tumor and peritumor regions for EB extravasation analysis at the advanced tumor stage. Quantitative analysis was conducted by measuring the increased EB extravasation of perivascular region based on an exponential recovery model (Fig. 4e and f). The representative results showed that the amount of dye extravasated out of the vessels in the tumor region was less than that in the peritumor region at first, while higher signals were observed starting at 65 min after EB injection, ultimately leading to an 86.9% higher extravasation at 120 min in the tumor region (Fig. 4f). The corresponding time-dependent EB extravasation rate can also be calculated in Fig. 4g by taking the first-order derivative of the exponential-fitted curve from Fig. 4f. Interestingly, the dye extravasation in the peritumor region started at a higher rate compared to that in the tumor region (1.1 versus 0.5). However, the extravasation rate surpassed that in the peritumor region at 35 min after injection and sustained at a higher level. The steady-state of the tumor region was not reached until 120 min, while the diffusion rate in the peritumor region dropped to less than 31.8% of the initial rate, tending to a steady-state. The imaging results of other mice can be found in the Fig. S14-S16. By quantitatively analyzing the EB leakage of the two stages, our PAM method can differentiate the BBB dysfunction in the tumor progression. It is noted that the PA signal remained stable in the cortical vessels of the advanced tumor during the imaging (Fig. 4h).

Probing immune microenvironment of orthotopic glioblastoma model

The therapeutic effect of emerging immunotherapy for GBM is associated with the tumor immune environment. A NIR-II photoacoustic sensor was developed for TAMCs targeting and dual-wavelength PAI. The A1094 dye with strong absorption (970-1200 nm, peak at 1094 nm) was synthesized according to reported methods. However, the strict hydrophobicity, poor biocompatibility, and non-specificity of the dye severely restricted its biological application. We loaded the dye with HSA to overcome the dilemmas. The highly expressed marker integrin CD11b (also known as αM-integrin or Mac^{-1}) on TAMCs was selected as a target via anti-CD11b antibodies (αCD11b) [38, 39]. Finally, an αCD11b-HSA@A1094 probe for TAMCs targeting was successfully fabricated by self-assembly of A1094 with proteins via chemical coupling and supramolecular interaction.

We established a theoretical modeling to stimulate the molecular docking process of αCD11b-HSA@A1094 probe, which showed the potential of binding residues and active pockets among A1094, albumin, and αCD11b (Fig. 5a and Fig. S18). The results showed that A1094 entered into the binding site of HSA through hydrophobic and van der Waals forces. For instance, the amino acid residue ASN192 on αCD11b formed 2.9, 2.6, and 3.3 Å lengths of hydrogen bonds with ALA504, PHE507, and PHE509 on HSA, respectively. Transmission electron microscopy (TEM) and dynamic light scattering (DLS) analysis showed that the probe was monodispersed spheres with an average size of 105 nm. The surface potential of HSA@A1094 complex changed considerably from -26.2 to -14.2 mV before and after the αCD11b modification (Fig. S19). The results indicated the successful fabrication of αCD11b-HSA@A1094. We measured the molar extinction spectrum of the probe and compared it with the hemoglobin absorption spectrum. The probe exhibited several orders of magnitude of higher absorption properties than hemoglobin in NIR-II region, which avoided the major absorption of tissue components (Fig. 5b). From the absorption spectrum, the peak of probe widened notably, but the positions did not change compared to A1094 dye (Fig. 5c and Fig. S20). The probe exhibited a good linear relationship between the PA amplitude and concentration (Fig. 5d). The fluorescence spectrum of probe was also characterized, which showed a weak emission peak at 585 nm and little emissions in the NIR-II window (Fig. S21). With an average laser fluence of 18.5 mJ/cm^2 at 1200 nm, both A1094 dye and the probe showed no visible PA amplitude change after 500 laser pulses irradiation, indicating fairly good stability (Fig. 5e). The small fluctuations were primarily attributed to the laser output itself. These results suggested the probe may act as excellent photoacoustic agents in the NIR-II optical window.

In a phantom test, cell inclusions containing different concentrations of labeled macrophages were injected into the tunnels of an agar-based phantom. The mean PA amplitude increased linearly with the concentration of labeled cells (Fig. S22). The detection limits of both PACT and PAM systems were calculated to be 3.125×10^3 cells/μL that corresponds to 980 and 31 cells in the analyzed volume of interest, respectively. *In vitro* targeting efficiency test was performed on murine macrophage cell line RAW264.7 and U87MG by confocal laser scanning microscopy and flow cytometry, the higher fluorescence intensity was detected 1 hour after probe incubation compared to controls (Fig. S23). Based on *in vivo* serum biochemistry and histopathological examinations, both the liver and kidney function indexes of ALT, ALP, AST, and UREA were stable and compatible after αCD11b-HSA@A1094 injection. Together with H&E staining in the main organs, the low toxicity and superior biosafety of probe were demonstrated for *in vivo* application (Fig. S24).

We further examined the feasibility of the probe for GBM tumor models *in vivo* by a commercial PACT system (LAZR-X, Vevo, Fujifilm, Japan). Tumor-bearing mice were intravenously injected with the probe and the PACT imaging was performed on cortex at different time points. MRI images were used as an auxiliary verification tool for GBM tumors at different stages, the current tumor status was confirmed by the corresponding MRI images in both groups, as shown in Fig. S25. A portable linear probe on this system was used to observe the cerebral vessel and TAMCs infiltration with laser wavelengths of 970 and 1200 nm, accordingly. The three-dimensional reconstructed images were collected by PACT before probe

injection to show PA contrast of blood at 970 nm and 1200 nm (Fig. S26). The scanning area on the cerebral surface was indicated by the red dashed box in Fig. 5f. Time-lapse PA images at 1200 nm showed an intuitive image contrast of TAMCs infiltration on the tumor-bearing mouse brain (Fig. 5g). The αCD11b-HSA@A1094 probe exhibited significant PA signal enhancement and longer retention time in the tumor region than HSA@A1094 complex. The PA amplitude of the HSA@A1094 group approached the maximum at 4 hours, then decreased and approached the initial level within 12 hours. The probe group had a significantly higher PA amplitude compared to the control group after 8 hours of injection and peaked at 12 hours (Fig. 5h). Therefore, the prolonged retention time of the probe can be used to distinguish TAMCs specifically. Ultrasound imaging and dual-wavelength PAI co-revealed tumor transplantation site, vascular morphology, and TAMCs infiltration (Fig. 5i). Biodistribution in major organ and brain of αCD11b-HSA@A1094 was also systematically investigated at 24 hours post-injection by fluorescence imaging (Fig. S27). The harvested brain was made into tissue slices for fluorescent microscopic analysis and histopathological examination (Fig. S28). To confirm the infiltration of $CD11b^+$ cells in the tumor region relative to normal brain tissue, immunohistochemistry was also performed (Fig. S29). These results indicated that the availability and safety of the probe for brain tumor TAMCs infiltration revealing *in vivo*.

Immune microenvironment visualization on micron level

Biomedical single wavelength PAM has been proven to be a powerful tool for exquisite high-resolution three-dimensional (3D) cerebrovascular imaging *in vivo*. Herein, we used a dual-wavelength (532 and 1064 nm) MEMS-based PAM to visualize vessels and TAMCs at the capillary level. In the phantom test, the PA amplitude had a good linear relationship with the concentration of the probe, indicating excellent detection stability and sensitivity (Fig. 6a and Fig. S16). The focal length shift was corrected on the leaf phantom experiments before *in vivo* dual-wavelength imaging (Fig. S2c, d). To test the imaging capability *in vivo*, two-wavelength PAI was performed on the cerebral cortex of tumor-bearing mice within 30 min of αCD11b-HSA@A1094 injection, successively (Fig. 6b, c). The probe entered the blood circulation by intravenous injection and selectively accumulated over time at the tumor region. By comparing the 532 and 1064 nm MAP images, both abnormal vascular morphology and spatial distribution in the tumor region were clearly indicated, the vessels in 1064 nm image were well lightened by the probe. The tumor region showed more complicated vessel arrangement and dense density.

Besides, to accurately present the changes of vessels and TAMCs infiltration during tumor progression, orthotopic GBM tumors caused alterations were revealed at two selective stages. By comparison, after 12 hours of probe injection, X-Z and X-Y MAP images from Day 12 and Day 18 post-inoculation indicated the differences in depth and range of TAMCs infiltration. From different perspectives, the different PA contrast and coverage range of the two stages indicated that TAMCs infiltration expanded heterogeneously with tumor progression as indicated by the white dashed circle (Fig. S5d, e, and Supplementary Video 1). We observed a comparable increase of TAMCs infiltration with tumor progression. To reveal the relative spatial location of vessels and TAMCs, the volume-rendered 3D images were performed by using the sequential acquisition of dual-wavelength images, in which morphological

vessels were rendered in red and fused with TAMCs in jet color (Fig. 6f, g). However, dual-wavelength fusion images obtained in HSA@A1094 complex injection group did not show indicative contrast of TAMCs in the tumor region (Fig. S30). This PAM approach, therefore, represented a straightforward and high-resolution imaging tool for obtaining unique cortex vasculature and TAMCs contrast revealing.

Conclusion

We present a comprehensive multi-feature photoacoustic molecular imaging approach for GBM studies, including angiogenesis, blood-brain barrier, and immune microenvironment. Compared with existing clinical imaging modalities, our PAI approach empowers high contrast and multicomponent visualization from the whole to a specific part of cerebral cortex. The dual-wavelength method avoids a large-scale inverse problem of considerable computational burden and error in conventional spectral unmixing approach. In dual-wavelength fusion imaging, although we successfully visualize abnormal vessels and immune microenvironment in the tumor-bearing brain, the detection sensitivity of the system can still be further improved by PA wavelength and hardware optimization. We have been able to monitor multiple vascular structural parameters in the GBM malignant progression. The microcirculation abnormality is also an important indicator of tumor progression.

Limited by pulse repetition frequency of the laser and B-scan rate, our system is currently insufficient to measure arterial and venous blood flow velocity in the tumor region. MEMS-PAM has great potential to diagnose the abnormality by visualizing and quantifying microvascular blood flow. To further improve the imaging speed while ensuring stability is our next-step goal. For further study, more information from the deeper brain could be described by cooperating with lower-frequency ultrasonic transducers of PACT. Functional imaging such as blood oxygen saturation can also be added to the multi-feature analysis approach. We expect this work will elicit broad interest from many research fields, including preclinical tumor diagnosis, anti-angiogenic strategies, and emerging immune-related therapies.

Declarations

Author contribution

JZ, XS and HL contributed equally to this work. All authors contributed to the study conception and design. Material preparation, data collection and analysis were performed by JZ, XS and HL. The first draft of the manuscript was written by JZ and LN, all authors commented on previous versions of the manuscript. All authors read and approved the final manuscript.

Funding

This research was supported by National Science Foundation of China (81922034).

Supporting Information

Supporting Information is available from the Wiley Online Library or from the author.

Ethics approval

Not applicable.

Consent to participate

Not applicable

Conflict of Interest

The authors declare no conflicts of interest.

Data Availability Statement

Data underlying the results presented in this paper are not publicly available at this time but may be obtained from the authors upon reasonable request.

Authors and Affiliations

[1]Departments of the State Key Laboratory of Molecular Vaccinology and Molecular Diagnostics & Center for Molecular Imaging and Translational Medicine, School of Public Health, Xiamen University, Xiamen, 361102 China.

[2]Research Center of Medical Sciences, Guangdong Provincial People's Hospital, Guangdong Academy of Medical Sciences, Guangzhou 510080, China.

References

1. Li YM, Suki D, Hess K, Sawaya R. The influence of maximum safe resection of glioblastoma on survival in 1229 patients: Can we do better than gross-total resection? J Neurosurg. 2016;124:977–88. doi:10.3171/2015.5.JNS142087.
2. Wen PY, Reardon DA. Neuro-oncology in 2015: Progress in glioma diagnosis, classification and treatment. Nat Rev Neurol. 2016;12:69–70. doi:10.1038/nrneurol.2015.242.
3. Norden AD, Drappatz J, Wen PY. Novel anti-angiogenic therapies for malignant gliomas. Lancet Neurol. 2008;7:1152–60. doi:10.1016/S1474-4422(08)70260-6.
4. Osswald M, Blaes J, Liao Y, Solecki G, Gommel M, Berghoff AS, et al. Impact of Blood-Brain Barrier Integrity on Tumor Growth and Therapy Response in Brain Metastases. Clin Cancer Res. 2016;22:6078–87. doi:10.1158/1078-0432.CCR-16-1327.
5. Sarkaria JN, Hu LS, Parney IF, Pafundi DH, Brinkmann DH, Laack NN, et al. Is the blood-brain barrier really disrupted in all glioblastomas? A critical assessment of existing clinical data. Neuro Oncol. 2018;20:184–91. doi:10.1093/neuonc/nox175.

6. Yang AC, Stevens MY, Chen MB, Lee DP, Stahli D, Gate D, et al. Physiological blood-brain transport is impaired with age by a shift in transcytosis. Nature. 2020;583:425–30. doi:10.1038/s41586-020-2453-z.
7. Pitz MW, Desai A, Grossman SA, Blakeley JO. Tissue concentration of systemically administered antineoplastic agents in human brain tumors. J Neurooncol. 2011;104:629–38. doi:10.1007/s11060-011-0564-y.
8. Manaenko A, Chen H, Kammer J, Zhang JH, Tang J. Comparison Evans Blue injection routes: Intravenous versus intraperitoneal, for measurement of blood-brain barrier in a mice hemorrhage model. J Neurosci Methods. 2011;195:206–10. doi:10.1016/j.jneumeth.2010.12.013.
9. Niu G, Lang L, Kiesewetter DO, Ma Y, Sun Z, Guo N, et al. In Vivo Labeling of Serum Albumin for PET. J Nucl Med. 2014;55:1150–6. doi:10.2967/jnumed.114.139642.
10. Quail DF, Joyce JA. The Microenvironmental Landscape of Brain Tumors. Cancer Cell. 2017;31:326–41. doi:10.1016/j.ccell.2017.02.009.
11. Hambardzumyan D, Gutmann DH, Kettenmann H. The role of microglia and macrophages in glioma maintenance and progression. Nat Neurosci. 2016;19:20–7. doi:10.1038/nn.4185.
12. Klemm F, Maas RR, Bowman RL, Kornete M, Soukup K, Nassiri S, et al. Interrogation of the Microenvironmental Landscape in Brain Tumors Reveals Disease-Specific Alterations of Immune Cells. Cell. 2020;181:1643-60 e17. doi:10.1016/j.cell.2020.05.007.
13. Qin H, Wei G, Gwak D, Dong Z, Xiong A, Kwak LW. Targeting tumor-associated myeloid cells for cancer immunotherapy. Oncoimmunology. 2015;4:e983961. doi:10.4161/2162402X.2014.983761.
14. Sica A, Porta C, Morlacchi S, Banfi S, Strauss L, Rimoldi M, et al. Origin and Functions of Tumor-Associated Myeloid Cells (TAMCs). Cancer Microenviron. 2012;5:133–49. doi:10.1007/s12307-011-0091-6.
15. Veglia F, Perego M, Gabrilovich D. Myeloid-derived suppressor cells coming of age. Nat Immunol. 2018;19:108–19. doi:10.1038/s41590-017-0022-x.
16. Pyonteck SM, Akkari L, Schuhmacher AJ, Bowman RL, Sevenich L, Quail DF, et al. CSF-1R inhibition alters macrophage polarization and blocks glioma progression. Nat Med. 2013;19:1264–72. doi:10.1038/nm.3337.
17. Cantero D, Rodriguez de Lope A, Moreno de la Presa R, Sepulveda JM, Borras JM, Castresana JS, et al. Molecular Study of Long-Term Survivors of Glioblastoma by Gene-Targeted Next-Generation Sequencing. J Neuropathol Exp Neurol. 2018;77:710–6. doi:10.1093/jnen/nly048.
18. Ntziachristos V. Going deeper than microscopy: the optical imaging frontier in biology. Nat Methods. 2010;7:603–14. doi:10.1038/nmeth.1483.
19. Zhang YS, Yao J. Imaging Biomaterial-Tissue Interactions. Trends Biotechnol. 2018;36:403–14. doi:10.1016/j.tibtech.2017.09.004.
20. Brenner DJ, Hall EJ. Computed tomography–an increasing source of radiation exposure. N Engl J Med. 2007;357:2277–84. doi:10.1056/NEJMra072149.

21. Schambach SJ, Bag S, Schilling L, Groden C, Brockmann MA. Application of micro-CT in small animal imaging. Methods. 2010;50:2–13. doi:10.1016/j.ymeth.2009.08.007.
22. Duyn JH. Studying brain microstructure with magnetic susceptibility contrast at high-field. NeuroImage. 2018;168:152–61. doi:10.1016/j.neuroimage.2017.02.046.
23. Li W, Chen R, Lv J, Wang H, Liu Y, Peng Y, et al. In Vivo Photoacoustic Imaging of Brain Injury and Rehabilitation by High-Efficient Near-Infrared Dye Labeled Mesenchymal Stem Cells with Enhanced Brain Barrier Permeability. Adv Sci (Weinh). 2018;5:1700277. doi:10.1002/advs.201700277.
24. Lv J, Xu Y, Xu L, Nie L. Quantitative Functional Evaluation of Liver Fibrosis in Mice with Dynamic Contrast-enhanced Photoacoustic Imaging. Radiology. 2021;300:89–97. doi:10.1148/radiol.2021204134.
25. Yao J, Wang L, Yang JM, Maslov KI, Wong TT, Li L, et al. High-speed label-free functional photoacoustic microscopy of mouse brain in action. Nat Methods. 2015;12:407–10. doi:10.1038/nmeth.3336.
26. Zhao H, Ke Z, Yang F, Li K, Chen N, Song L, et al. Deep Learning Enables Superior Photoacoustic Imaging at Ultralow Laser Dosages. Adv Sci (Weinh). 2021;8:2003097. doi:10.1002/advs.202003097.
27. Chen R, Huang S, Lin T, Ma H, Shan W, Duan F, et al. Photoacoustic molecular imaging-escorted adipose photodynamic-browning synergy for fighting obesity with virus-like complexes. Nat Nanotechnol. 2021;16:455–65. doi:10.1038/s41565-020-00844-6.
28. Zhao H, Chen N, Li T, Zhang J, Lin R, Gong X, et al. Motion Correction in Optical Resolution Photoacoustic Microscopy. IEEE Trans Med Imaging. 2019;38:2139–50. doi:10.1109/TMI.2019.2893021.
29. Baik JW, Kim JY, Cho S, Choi S, Kim J, Kim C. Super Wide-Field Photoacoustic Microscopy of Animals and Humans In Vivo. IEEE Trans Med Imaging. 2020;39:975–84. doi:10.1109/TMI.2019.2938518.
30. Kim JY, Lee C, Park K, Lim G, Kim C. Fast optical-resolution photoacoustic microscopy using a 2-axis water-proofing MEMS scanner. Sci Rep. 2015;5:7932. doi:10.1038/srep07932.
31. Park K, Kim JY, Lee C, Jeon S, Lim G, Kim C. Handheld Photoacoustic Microscopy Probe. Sci Rep. 2017;7:13359. doi:10.1038/s41598-017-13224-3.
32. Yao J, Huang CH, Wang L, Yang JM, Gao L, Maslov KI, et al. Wide-field fast-scanning photoacoustic microscopy based on a water-immersible MEMS scanning mirror. J Biomed Opt. 2012;17:080505–1. doi:10.1117/1.JBO.17.8.080505.
33. Nie L, Huang P, Li W, Yan X, Jin A, Wang Z, et al. Early-stage imaging of nanocarrier-enhanced chemotherapy response in living subjects by scalable photoacoustic microscopy. ACS Nano. 2014;8:12141–50. doi:10.1021/nn505989e.
34. Wu Z, Duan F, Zhang J, Li S, Ma H, Nie L. In vivo dual-scale photoacoustic surveillance and assessment of burn healing. Biomed Opt Express. 2019;10:3425–33. doi:10.1364/BOE.10.003425.

35. Tian M, Tatsuura S, Furuki M, Sato Y, Iwasa I, Pu LS. Discovery of novel dyes with absorption maxima at 1.1 microm. J Am Chem Soc. 2003;125:348–9. doi:10.1021/ja0209666.
36. Yao J, Maslov K, Hu S, Wang LV. Evans blue dye-enhanced capillary-resolution photoacoustic microscopy in vivo. J Biomed Opt. 2009;14:054049. doi:10.1117/1.3251044.
37. Quail DF, Joyce JA. Microenvironmental regulation of tumor progression and metastasis. Nat Med. 2013;19:1423–37. doi:10.1038/nm.3394.
38. Nigam S, McCarl L, Kumar R, Edinger RS, Kurland BF, Anderson CJ, et al. Preclinical ImmunoPET Imaging of Glioblastoma-Infiltrating Myeloid Cells Using Zirconium-89 Labeled Anti-CD11b Antibody. Mol Imaging Biol. 2020;22:685–94. doi:10.1007/s11307-019-01427-1.
39. Schmid MC, Khan SQ, Kaneda MM, Pathria P, Shepard R, Louis TL, et al. Integrin CD11b activation drives anti-tumor innate immunity. Nat Commun. 2018;9:5379. doi:10.1038/s41467-018-07387-4.

Figures

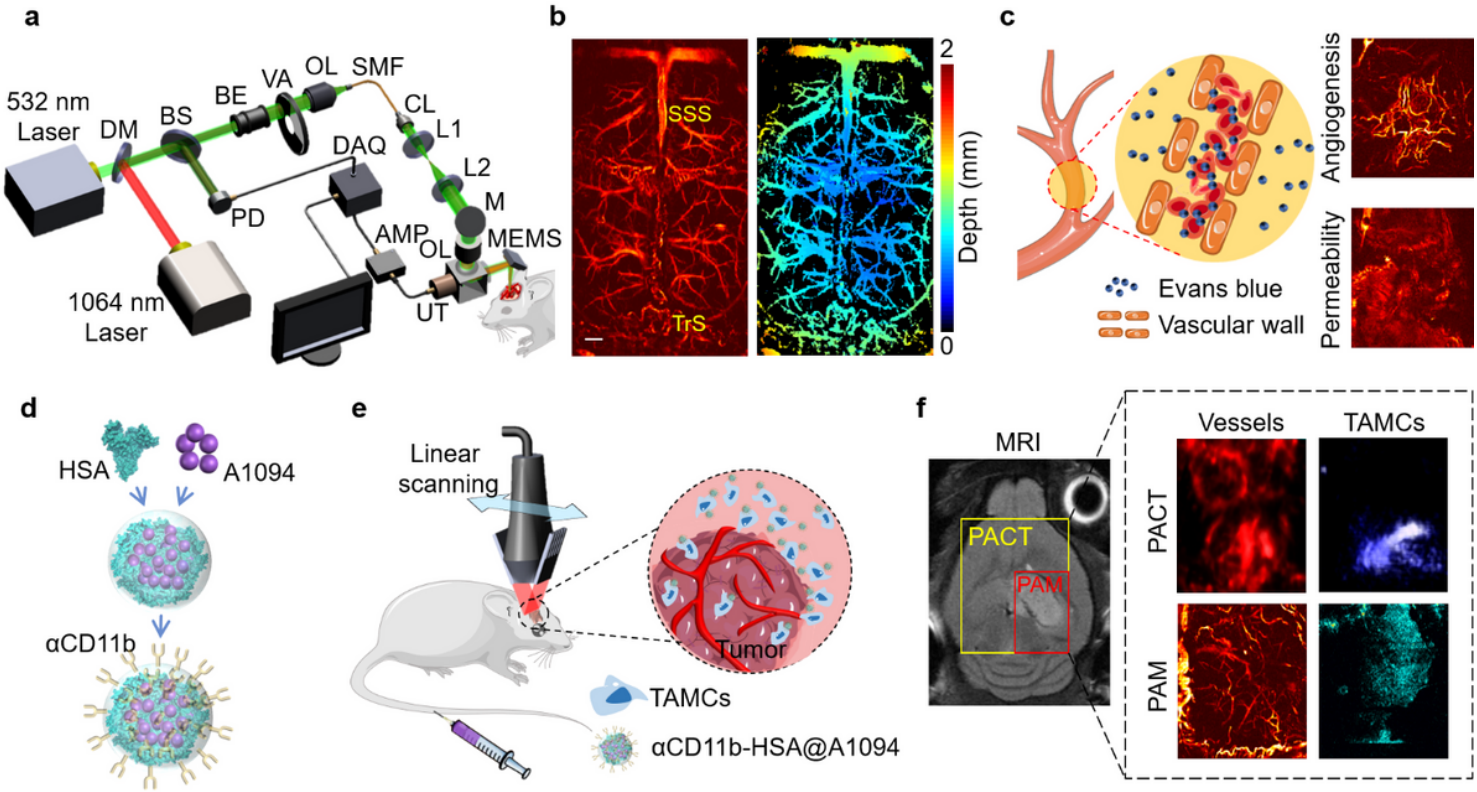

Figure 1

The dual-scale and multi-wavelength photoacoustic molecular imaging approach for *in vivo* assessment of GBM neovascularization and TAMCs. (a) Schematic of MEMS-based PAM system for transcranial imaging. DM, dichroic mirror; BS, beam splitter; PD, Photodiode; BE, beam expander; VA, variable attenuator; OL, objective lens; SMF, single-mode fiber; CL, collimating lens; M, mirror; UT, ultrasonic transducer; MEMS, microelectromechanical systems; AMP, amplifier; DAQ, data acquisition card. (b) Representative PAM image of normal mouse brain cortex and its depth encoding image (scale bar = 500

μm). (c) Imaging GBM neovascularization and vascular permeability changes by PAM. (d) A brief synthesis diagram of TAMCs targeted nanoprobe, αCD11b-HSA@A1094. (e) Schematic diagram of TAMCs tracing by PACT in an orthotopic GBM model. (f) The distribution of cerebral cortex vessels and TAMCs by dual-wavelength PACT (970 and 1200 nm) and PAM (532 and 1064 nm) approaches (yellow and red boxes in the MRI image indicated the imaging region of PACT and PAM, respectively). SSS, superior sagittal sinus; TrS, transverse sinus; HSA, human serum albumin; TAMCs, tumor-associated myeloid cells.

Figure 2

Morphological changes of blood vessels caused by tumor progression. (a) *In vivo* T2-weighted MRI images of GBM-bearing mice at Day 7, 12, and 18 after tumor cell implantation with detailed structural information of cortex. The red dashed box indicates the tumor region. (b) Vessel network in tumor region at different stages obtained by PAM at 532 nm (acquisition time ~60 s). (c-f) Quantitative vessel network analysis of region I (green dashed box) and II (blue dashed box) in (b), four indicators included total number of vessels (c), density (d), branch points (e), and tortuosity (f) were counted, statistical comparison with the paired t-test, ns, *, and **, respectively represent no significance, $p < 0.05$, and $p < 0.01$ ($n = 5$ for each group). (g) Vessel distribution images in the whole cerebral cortex of normal and tumor-bearing mice obtained by PACT at 800 nm. (h) Vascular morphology images along the sagittal suture of normal and tumor-bearing mice obtained by PAM at 532 nm (acquisition time ~100 s). All statistical data are expressed as mean ± SD.

Figure 3

In vivo Detection of BBB permeability by EB staining. (a) MRI image of GBM-bearing mouse brain at Day 7. (b) PA image of the brain cortex acquired in the yellow dashed box of (a) by PAM at 24 h after EB injection. The diffuse signal indicated EB extravasation from the vessels. Less EB staining was evident in the brain tissue. (c) PA amplitude profile of (b). (d) Photograph of *ex vivo* brain tissues. (e-h) Corresponding results of GBM-bearing mouse brain at Day 18. Areas of “bluing” in photos represent that the vascular permeability to EB-albumin complex increased with tumor progression. (i) PA images of the mice in the early-stage group. (j) PA images of the mice in the middle-stage group. (k) PA images of the mice in the advanced-stage group.

Figure 4

The evaluation of tumor caused BBB dysfunction. (a-b) Time-lapse monitoring of BBB status in early (Day 7) and advanced (Day 18) stage of tumor-bearing mice by PAM at 532 nm, n=4 for each group, acquisition time ~80 s, (scale bar = 500 μm). (c-d) Spatiotemporal distribution of the EB dye leakage of (a) and (b) group along the three white dashed lines. (e) Magnified views of the blue and green and blue dashed boxes from (b) at 120 min, the typical spatial distribution of the extravascular EB at peritumor and tumor regions, scale bar = 500 μm. (f) Comparison of EB extravasation dynamics in the peritumor and tumor regions. The data points are the averages. (g) Corresponding diffusion rate over time. (h) The PA signals in the vessels of advanced tumors (Day 18) remained stable within two hours.

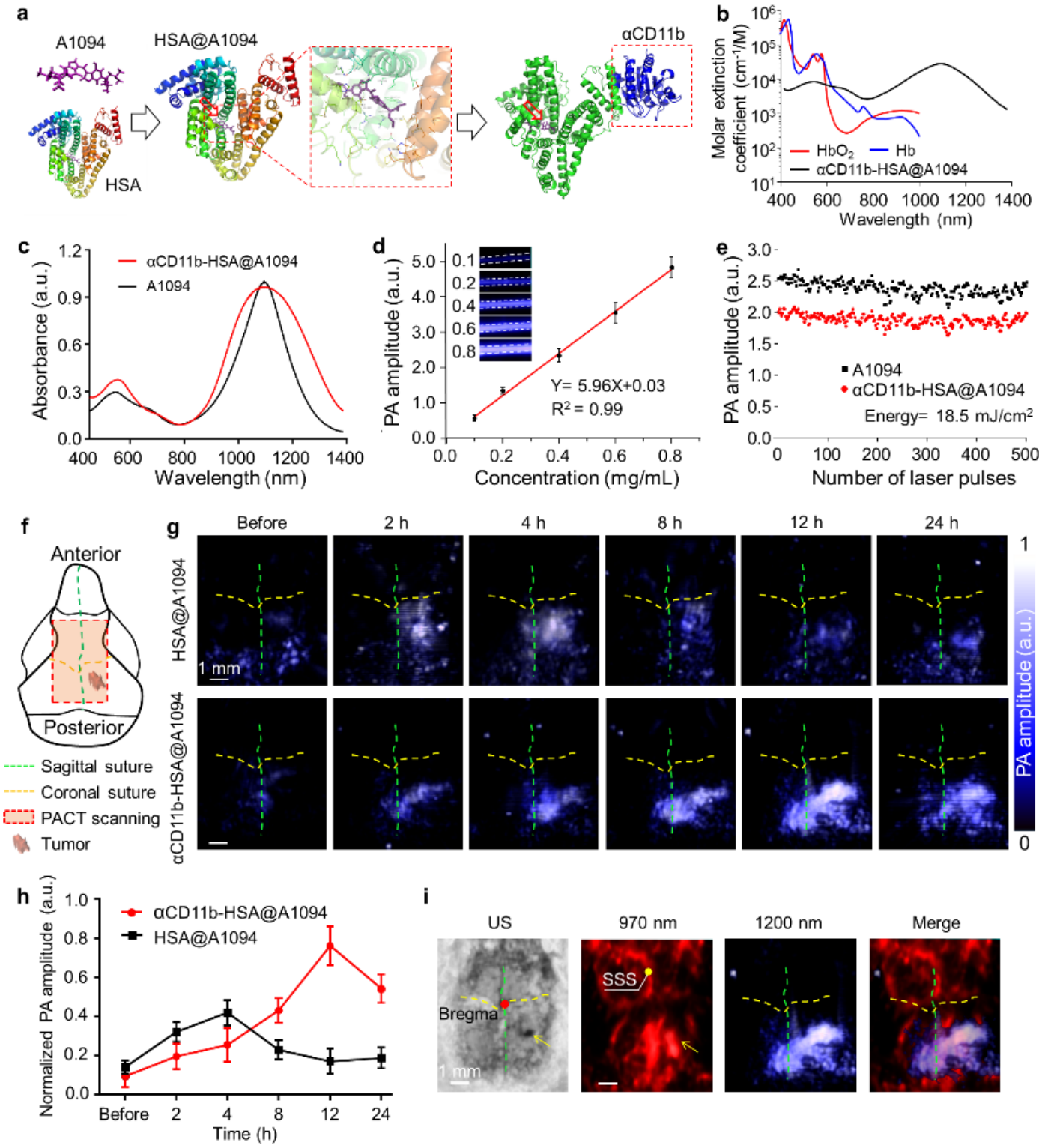

Figure 5

The synthesis route of αCD11b-HSA@A1094 nanoprobe and photoacoustic performance test by PACT. (a) Scheme for the formation of the αCD11b-HSA@A1094 probe. (b) Molar extinction spectra of hemoglobin and probe. (c) Absorption spectra of A1094 dye and nanoprobe. (d) PA amplitude of nanoprobe at 1200 nm as a function of concentration. (e) Photoacoustic stability test of A1094 dye and probe illuminated with 500 laser pulses at 1200 nm with 18.5 mJ/cm^2. (f) Schematic diagram of mouse

skull structure and imaging region by PACT, PA area: 7 mm × 8 mm. (g) *In vivo* evaluation of the nanoprobe accumulation in orthotopic GBM at 1200 nm after intravenous injection of probe at indicated time points (n=4 for each group), acquisition time ~2.5 min. (h) The quantitative PA amplitude changes of (g). (i) Ultrasound imaging and NIR dual-wavelength PA images of tumors. The dual-wavelength PA images showed cortex vessels (970 nm) and TAMCs distribution (1200 nm), simultaneously. All statistical data are expressed as mean ± SD.

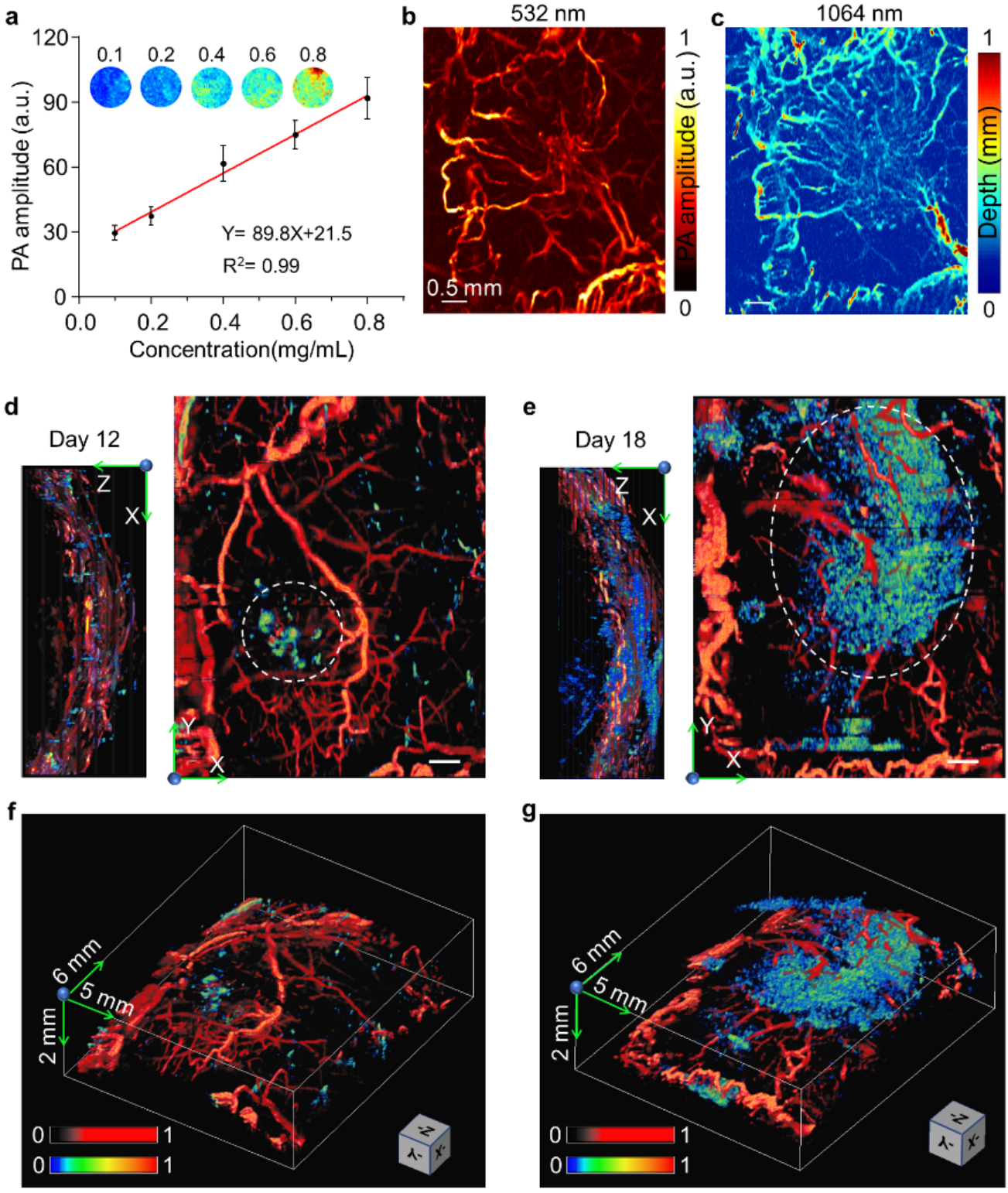

Figure 6

Images of the tumor-bearing mouse brain by dual-wavelength MEMS-based PAM. (a) PA amplitude of αCD11b-HSA@A1094 at 1064 nm as a function of concentration. (b-c) Dual-wavelength (532 and 1064 nm) MAP images of the vascular morphology in 30 min after intravenous injection (acquisition time ~60 s). (d-e) Multiple views (X-Y, X-Z plane) of the TAMCs surrounded by the vasculature in the cerebral cortex acquired at 12 hours after αCD11b-HSA@A1094 injection on Day 12 (d) and Day 18 (e) of tumor

progression, scale bar = 500 μm. (f-g) Corresponding volume-rendered 3D fusion images with dimensions of 6 mm × 5 mm × 2 mm.

Supplementary Files

This is a list of supplementary files associated with this preprint. Click to download.

- SI.docx
- SupplementaryMovie.mp4